ACS APPLIED MATERIALS & INTERFACES

www.acsami.org Research Article

Solvent Vapor Annealing, Defect Analysis, and Optimization of Self-Assembly of Block Copolymers Using Machine Learning Approaches

Gayashani Ginige, Youngdong Song, Brian C. Olsen, Erik J. Luber,* Cafer T. Yavuz, and Jillian M. Buriak*

Cite This: *ACS Appl. Mater. Interfaces* 2021, 13, 28639−28649

Read Online

ACCESS | Metrics & More | Article Recommendations | Supporting Information

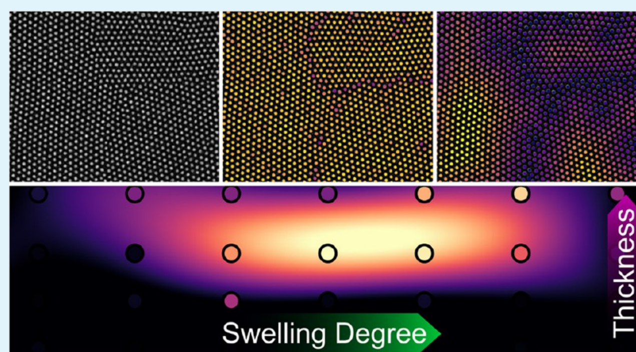

ABSTRACT: Self-assembly of block copolymers (BCPs) is an alternative patterning technique that promises high resolution and density multiplication with lower costs. The defectivity of the resulting nanopatterns remains too high for many applications in microelectronics and is exacerbated by small variations of processing parameters, such as film thickness, and fluctuations of solvent vapor pressure and temperature, among others. In this work, a solvent vapor annealing (SVA) flow-controlled system is combined with design of experiments (DOE) and machine learning (ML) approaches. The SVA flow-controlled system enables precise optimization of the conditions of self-assembly of the high Flory−Huggins interaction parameter (χ) hexagonal dot-array forming BCP, poly(styrene-*b*-dimethylsiloxane) (PS-*b*-PDMS). The defects within the resulting patterns at various length scales are then characterized and quantified. The results show that the defectivity of the resulting nanopatterned surfaces is highly dependent upon very small variations of the initial film thicknesses of the BCP, as well as the degree of swelling under the SVA conditions. These parameters also significantly contribute to the quality of the resulting pattern with respect to grain coarsening, as well as the formation of different macroscale phases (single and double layers and wetting layers). The results of qualitative and quantitative defect analyses are then compiled into a single figure of merit (FOM) and are mapped across the experimental parameter space using ML approaches, which enable the identification of the narrow region of optimum conditions for SVA for a given BCP. The result of these analyses is a faster and less resource intensive route toward the production of low-defectivity BCP dot arrays via rational determination of the ideal combination of processing factors. The DOE and machine learning-enabled approach is generalizable to the scale-up of self-assembly-based nanopatterning for applications in electronic microfabrication.

KEYWORDS: *block copolymer, self-assembly, defect density, solvent vapor annealing, process control, directed self-assembly, memory, machine learning, high throughput*

Downloaded via KING ABDULLAH UNIV SCI TECHLGY on February 10, 2022 at 07:41:23 (UTC).
See https://pubs.acs.org/sharingguidelines for options on how to legitimately share published articles.

INTRODUCTION

The spontaneous self-assembly of block copolymers (BCPs) to generate patterns and motifs with high resolution at low cost has been of great interest for over two decades as an alternative or complementary technique to photolithography.[1−6] When integrated with sparse guiding morphological or chemical features produced via traditional lithography, these low-cost polymer processing methods enable the generation of templates for the production of sub-10 nm features with a high degree of long-range order.[7] This combination of self-assembly with lithography is termed directed self-assembly (DSA) and has been primarily directed toward applications in microelectronics, including memory storage materials,[3,8] finFET,[2,9] and vias.[10,11] These nanopatterned substrates have also seen use as catalysts for growth of ordered nanowire arrays[12,13] and as platforms for a diverse array of applications, including protein detection,[14,15] separation membranes,[16,17] surface-enhanced Raman spectroscopy (SERS) substrates,[18,19] anti-reflective coatings in photovoltaics,[20,21] and chemical and biomedical sensors.[22,23]

The self-assembly of a monolayer of a given BCP on a flat, featureless surface results in a polycrystalline morphology with uncorrelated nano- to micron-sized domains, with a significant concentration of defects.[24] The ITRS (now IDRS roadmap) has specified a target of a maximum defectivity of ~1 per 100 cm^{-2},[25−28] which is several orders of magnitude lower than that quantified in patterns derived from these monolayers of

Received: March 17, 2021
Accepted: May 25, 2021
Published: June 8, 2021

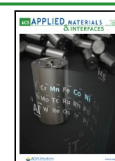

© 2021 American Chemical Society

https://doi.org/10.1021/acsami.1c05056
ACS Appl. Mater. Interfaces 2021, 13, 28639−28649

self-assembled BCPs on substrates lacking guiding patterns. Some kinetically trapped nonequilibrium metastable configurations in the free energy landscape persist even through long annealing times, which is an issue for high volume manufacturing on 300 mm wafers.[7,11,27,29] In an attempt to minimize defect formation during the course of self-assembly, much effort has been directed toward the optimization of annealing of the spin-coated BCP films, including solvent vapor,[30−32] thermal (including microwave irradiation),[33−35] a combination of solvent and thermal (solvothermal),[36,37] laser annealing,[38,39] shear flow,[40,41] and annealing within an electric field.[42] Lithography multiplication via DSA also reduces defect density as chemical and morphological features on the surface help in guiding the BCP into the lowest energy equilibrium patterns.[4,6,27] Significant progress has been made in recent years, where the defectivity of DSA is now considered within tolerance when combined with using extreme UV (EUV) or e-beam lithography.[1] However, there is still a pressing need to reduce the defectivity of unguided BCP films, as this would allow for the fabrication of larger spacings between guiding patterns and greatly reduce the cost and demands of the lithographic step. Moreover, defects still remain a challenge, however, particularly with smaller molecular weight BCPs with a high Flory−Huggins interaction parameter ($\chi_N > 10.5$) that produce the sub-20 nm periodicities[6,43,44] and features.[5]

To achieve the desired nanopattern via self-assembly, not only are the annealing parameters critical but the initial thickness of the applied BCP monolayer must be precise, typically within one or two nanometers.[7,45−50] The ideal thickness for a given BCP is unique and depends upon the composition of the BCP and factors such as surface functionalization and energy, the use of a topcoat, and other factors.[4,6,27,44,46,51] Both experimental and computational results strongly link initial film thickness with the resulting self-assembled structure and persistent defects.[11,52,53] Small fluctuations of thickness within a monolayer film can lead to different self-assembled structures as unfavorably thin domain thicknesses frustrate packing due to the buildup of strain.[25,53] The periodicity of structures formed from self-assembled BCP nanopatterns may be dependent upon film thickness and other processing parameters, as has been recently shown with bottlebrush BCPs.[45,54]

The defects observed in self-assembled monolayers of BCPs that form hexagonal dot patterns are dominated by disclinations and dislocations, as well as point defects along grain boundaries between uncorrelated domains, multilayers, and the presence of lamellae.[31,55−58] These hexagonal-dot-based nanopatterns are of interest for memory materials and devices, applications that are more tolerant of defects than linear patterns for CMOS (e.g., vias), and thus the route toward commercialization appears more direct.[1] "Further improvement of process-friendly techniques"[1] is, however, still required, particularly over large areas. With the optimization of self-assembly of any new BCP, particularly high-χ BCPs that may be challenging due to long-lived metastable defects, or any change in processing conditions, annealing parameters will need to be re-evaluated. Empirical optimization of annealing of BCP films is time consuming and if not rationally devised will incompletely sample variable space.[59,60] In an attempt to optimize these SVA parameters more efficiently with fewer laboratory resources (including time, one of the most precious resources), we use a full factorial experimental design complemented by machine learning (ML) approaches to identify the optimized SVA parameters. Prior to optimizing BCP dot arrays for minimum defectivity, we first define and expand the definition of what constitutes a defect beyond topological defects to encompass positional fluctuations, as many applications (such as bit-patterned media) are concerned with nanoscale positional accuracy. Then, we define a figure of merit (FOM) that encompasses defect density and the spatial distribution of these defects at all relevant length scales. However, the factors involved in solvent annealing are nonorthogonal and correlated, with one alteration affecting other parameters of the film during self-assembly and the effects playing out over different length scales. Given the difficulties of optimizing correlated systems with numerous input parameters, we show how ML techniques may be applied to map out and minimize the defect densities of solvent-annealed hexagonal dot-forming BCP nanopatterns. While this work focuses exclusively upon solvent vapor annealing of BCP films, the approach to optimization described here could be applied to other annealing methods.

EXPERIMENTAL METHODS

Materials. Poly(styrene-*b*-dimethylsiloxane) (43k-*b*-8.5k) diblock copolymer (PS-*b*-PDMS) with a polydispersity index of 1.04 was purchased from Polymer Source Inc. and used as is. Toluene (>99%) and tetrahydrofuran (THF, >99%) were obtained from Fisher Scientific. Silicon wafers [⟨100⟩, 4 in. diameter, thickness 525 ± 25 mm, p-type (boron doped), resistivity < 0.005 Ω·cm] were purchased from WRS Materials. Sulfuric acid (96%) and hydrogen peroxide (30%) were purchased from Avantor Performance Materials.

Silicon Wafer Dicing and Cleaning. Silicon wafers were diced into 1 cm × 1 cm squares by a DAD 321 dicing saw and cleaned in a freshly prepared piranha solution [3:1 v/v sulfuric acid (96%)/hydrogen peroxide (30%); *caution*: piranha solution violently reacts with organic matter] for 15 min and washed with DI water and dried in a nitrogen stream.

BCP Thin Film Self-Assembly. A bulk BCP solution with a concentration of 2 wt % in toluene was used to prepare solutions with concentrations ranging from 0.6 to 1.4 wt %. BCP thin films with thicknesses between 20 and 33 nm were prepared by spin-casting 25 μL of the desired polymer solution as shown in Figure S1 on piranha solution-cleaned Si chips at 8500 rpm for 40 s with a WS-400BZ-6NPP/120 LITE spin-coater (Laurell Technologies Corporation). The initial film thickness was measured by ellipsometry and is the average of ellipsometric measurements taken at five different points on the chip. The variation of thickness with the concentration of the BCP solution is shown in Figure S1.

Controlled Solvent Vapor Flow Annealing System. A complete procedure for the annealing of a thin film of BCP on an oxide-capped Si chip using the controlled solvent vapor flow annealing system has been previously described.[31] The initial film thickness (in nm) and target swelling degree (SD = swollen film thickness/initial film thickness) were entered into the program controlling the solvent annealing system. The dwell time was 300 s, and the ramp speed was 0.3 SD/min for all samples. It was ensured that the bubbler had enough solvent (THF) before commencing the annealing program, and 20 sccm (standard cubic centimeter per minute) of Ar was bubbled into the solvent bubbler along with another pure Ar mixer to adjust the value automatically. The program automatically stopped solvent vapor flow at the end of the annealing, and the BCP film was deswelled by purging the annealing chamber with pure Ar. The design, assembly, and application of this solvent vapor flow annealing system were described in detail in a previous methods and protocols article by our group.[31] Briefly, swelling degree is measured in situ and controlled via a feedback loop. As the volume of the annealing chamber is small, less than 1.5 cm^3, at a carrier gas flow rate of 20 sccm, full replacement of the volume of the annealing

https://doi.org/10.1021/acsami.1c05056
ACS Appl. Mater. Interfaces 2021, 13, 28639−28649

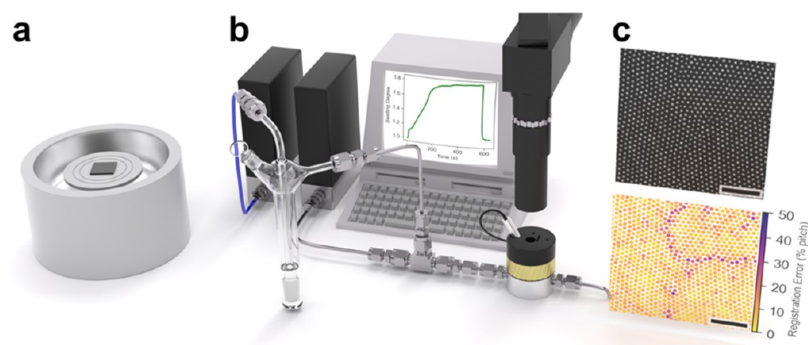

Figure 1. (a) Prior to solvent annealing the BCP film is spin-coated onto silicon, locking in the initial film thickness. (b) Solvent vapor annealing (SVA) to a predetermined swelling degree (SD) using a feedback-controlled annealing system. (c) Defect analysis of the resulting plasma-treated, silica nanopatterns imaged by SEM. Both scale bars are 250 nm.

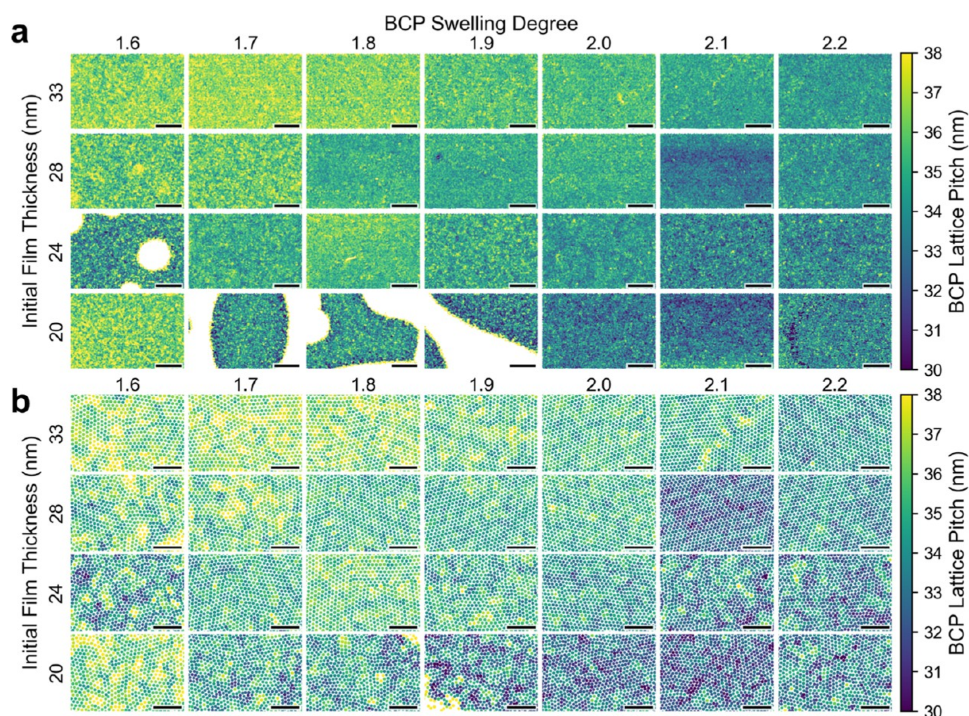

Figure 2. BCP lattice pitch as a function of SVA conditions. (a) Dot value maps showing dot locations for all 28 combinations of the initial thickness of the PS-*b*-PDMS films and swelling degrees, indicated by the labeled rows and columns, respectively, and showing color values for the BCP lattice pitch in nm. All scale bars are 1 μm. (b) Details of (a) showing individual dots. All scale bars are 250 nm.

chamber is complete within 4.5 s. This allows the films to be quenched to a swelling degree of less than 1.5 in under 2 s.

PS-*b*-PDMS Thin-Film Reactive Ion Etching (RIE) Process. All PS-*b*-PDMS thin films were etched with a Plasmalab μEtch RIE using a two-step etch: The first step removed the surface wetting layer of PDMS on the BCP film using a CF_4 plasma (100 sccm), 100 mT, 50 W, for 8 s. The second step, using an O_2 plasma (100 sccm), 135 mT, 30 W, for 60 s removed the PS and converted the PDMS block into SiO_x.

Film Characterization. High-magnification SEM micrographs were taken using a Hitachi S4800 scanning electron microscope (15 kV, 20 μA). Low-resolution micrographs were taken using a Zeiss Sigma field emission scanning electron microscope (15 kV, 20 μA).

Data Processing. SEM micrographs were processed to extract dot positions and areas of the single layer phase using Gwyddion image analysis software.[61] The background of the micrographs was removed using median scan line alignment followed by polynomial background removal and revolve arc for the single layer and dot micrographs, respectively. A Gaussian filter was then used to reduce high-frequency noise. The layer and dots were then marked by a brightness threshold determined using Otzu's method.[62] The ratio of the single layer area was then averaged over eight SEM micrographs for each set of conditions studied to get the final area percent of the single layer phase. The dot positions were used to compute the various metrics of the BCP dot arrays. The raw SEM micrographs for all SVA conditions, used to determine dot positions, are shown in Figure S2. The size and resolution for silica dot arrays are 4.57 μm × 3.05 μm and 3070 × 2045 pixels, respectively. For the phase images, the size is 127 μm × 89 μm and the resolution is 2560 × 1920 pixels.

The majority of the metrics used in this work are derived from the dot positions of the six nearest neighbors of each dot in relation to itself. The nearest neighbors are calculated using the ball tree algorithm in Scikit-learn.[63] The dot pitch of each dot is calculated from the mean distance of its six nearest neighbors to itself. The cell orientation angle of each dot is the circular mean of the angle of each nearest neighbor vector modulus with 60°. This gives a cell orientation angle from −30 to 30° for each dot. The registration error (R_e) is calculated from the six nearest neighbors as explained in the Supporting Information. Defect distance is defined as the shortest

https://doi.org/10.1021/acsami.1c05056
ACS Appl. Mater. Interfaces 2021, 13, 28639−28649

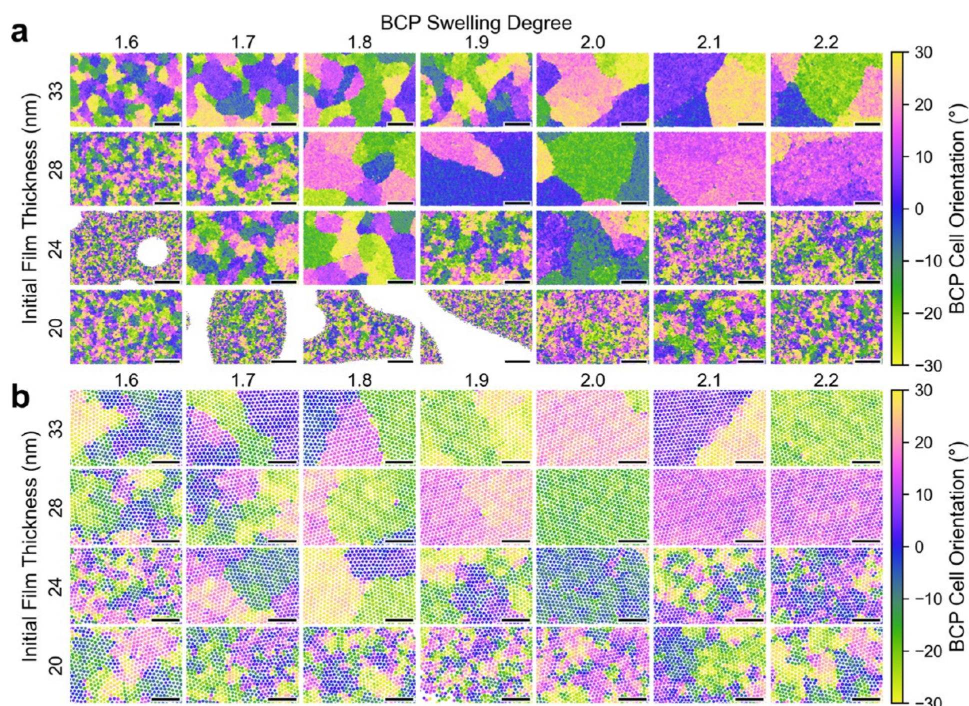

Figure 3. BCP lattice cell orientation as a function of SVA conditions. (a) Dot value maps showing dot locations for all 28 combinations of the initial thickness of the PS-*b*-PDMS films and swelling degrees, indicated by the labeled rows and columns, respectively, and showing color values for BCP lattice cell orientation in degrees. All scale bars are 1 μm. (b) Details of (a) showing individual dots. All scale bars are 250 nm.

distance from each dot to a defect. For the ML fit maps, the ensemble averages are taken as the mean of all nondefective dots.

ML fit maps were made to visualize the changes in the relevant metrics across all conditions tested. The fitting is performed using a radial basis function (RBF) kernel support vector machine (SVM) from Scikit-learn.[63] After fitting, the function is remapped onto a grid to form an image for visualization.

■ RESULTS AND DISCUSSION

In this work, we analyze the defects and associated distributions observed in different thicknesses of PS-*b*-PDMS thin films that are solvent-annealed to a range of swelling degrees, plasma-etched, and converted into silica nanopatterns, as outlined in Figure 1. This analysis of defects runs through a wide range of magnifications starting from defects in the lattice itself to grains to different macroscale phases in the film (wetting, single, and double layers).

The focus of this work is the quantification, prediction, and minimization of defect density at all length scales of dot-forming BCP films. However, other important metrics of the BCP dot array, such as pitch, can be easily determined and the effects of the solvent vapor annealing (SVA) parameter space on pitch can be analyzed. Shown in Figure 2 are dot maps of a localized BCP dot pitch, where the pitch of each dot is determined by taking the mean distance of a dot and its six nearest neighbors. From both the low (Figure 2a) and high (Figure 2b) magnification maps, we can see that there is a clear trend of a small decrease in pitch with increasing swelling degree. These maps are color-coded; thus, the shift in color from yellow-green to blue-green is showing a decrease of pitch as the degree of swelling increases. As the degree of swelling is raised from 1.6 to 2.2, the average values of the localized pitch-range drop from 36.5 nm to 32.5 nm (displayed graphically in Figure S3). Similar trends showing a decrease in pitch with increasing swelling degrees have been observed by others for different initial film thicknesses.[30,64] At first glance, it may seem somewhat counterintuitive that the pitch decreases as the swelling degree increases; however, it is important to realize that the film can only swell in the vertical direction perpendicular to the substrate, which causes the microdomains to become nonspherical where they shrink in size in the in-plane direction and stretch in the out-of-plane direction.[64] The decrease in pitch with increased swelling degree can be best understood by noting that the domain spacing, L, in the strong segregation limit is given by $L \sim N^{2/3}\chi_{\mathrm{eff}}^{1/6}$.[65,66] Given that the effective Flory−Huggins interaction parameter χ decreases linearly with the amount of solvent incorporated into the film,[64,67] the domain spacing is expected to decrease as swelling degree increases, as observed. Similarly, solvent molecules can fully incorporate into thinner films more easily compared to thicker films, leading to a decrease in pitch.[68] It is also worth noting that there are several blank/white patches in the films of thicknesses of 20.0 and 24.0 nm. These patches are wetting/lamellae phase layers that correspond to very thin regions of the BCP film.[31,56] These phases do not contain any dots/micelles and as such are left blank for all subsequent analyses.

Before quantitatively analyzing the defects in these BCP dot patterns, it is first useful to visualize the grain structures observed with different annealing conditions. The local cell orientation of each dot is mapped in Figure 3, which effectively maps out individual grains (regions where all of the BCP dots have the same relative orientation). These results clearly demonstrate the large variability in long-range ordering as a function of initial film thickness and swelling degree. Some films comprise many very small, sub-100 nm grains, and others are uniform over micron scales. At a film thickness of 20.0 nm, the annealed films have extremely small grains (on the order of a few lattice pitches) and the grains themselves have a low

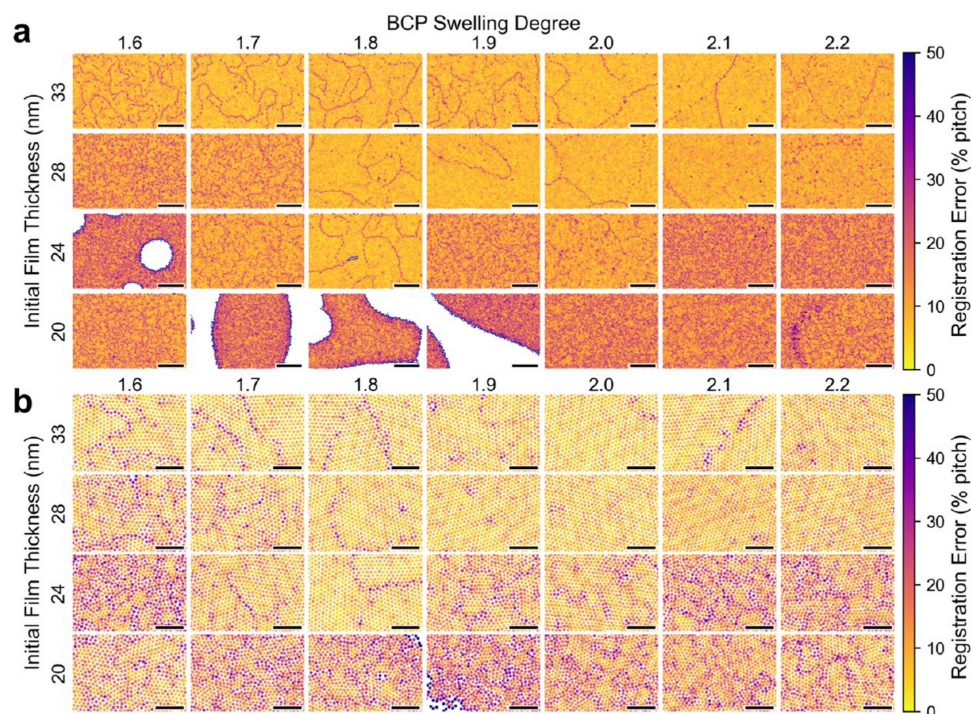

Figure 4. Registration error as a function of SVA conditions. (a) Dot value maps showing dot locations for all 28 combinations of the initial thickness of the PS-*b*-PDMS films and swelling degrees, indicated by the labeled rows and columns, respectively, and showing color values for registration errors in percent dot pitch. All scale bars are 1 μm. (b) Details of (a) showing individual dots. All scale bars are 250 nm.

degree of local orientational ordering (vide infra). There also appear to be regions of optimal grain size and local orientational ordering. For example, at an initial film thickness of 24.0 nm, the grain size increases as the swelling degree increases, reaching a maximum size, but then decreases as the swelling degree is further increased; the local ordering also seems to significantly decrease. The initial increase in grain size with increased swelling degree is a result of the intended action of solvent annealing, where increased solvent vapor incorporated into the film increases chain mobility, allowing for the formation of ordered lattice structures with lower configurational energy.[30] However, this increase in chain mobility is always accompanied by a decrease in segregation strength and thus as the segregation strength approaches the order–disorder transition (ODT) the local microdomain ordering begins to decrease.[30,69] These competing processes of chain mobility and segregation strength explain the trends observed in Figure 3 where there will be an optimal swelling degree for a given initial film thickness to maximize grain size and long-range ordering.

Although these BCP cell orientation maps provide a useful qualitative sense of grain size and long-range ordering, it is necessary to quantitatively define and measure defects to apply ML methods to optimize the SVA processing. One of the most conventional methods for identifying defects is the determination of the coordination number, where any non-6-fold coordinated dots are marked as defects.[70,71] Maps of the local coordination number are shown in Figure S4, which very clearly identify topological point defects like dislocations and disclinations having 5- and 7-fold coordinated sites. Although the coordination number very easily identifies point defects, it does not encode for fluctuations and deviations from perfect hexagonal coordination shells, which is a significant concern in these soft BCP lattices during SVA. These deviations from perfect hexagonal lattice positions are important to consider when attempting to quantify the defectivity of these BCP lattices and their broader applications in devices requiring nanoscale positional accuracy. Specifically, it is easy to imagine a lattice with only 6-fold coordinated sites but having sufficiently large local fluctuations in dot positioning to cause read/write errors. With this concept in mind, we define the metric of registration error (R_e) to identify fluctuational defects.

Simply put, the R_e of a given dot is a measure of the average distance of its six nearest neighbors from the corresponding perfect hexagonal coordination shell. Expressed mathematically, the R_e of any dot is given by

$$R_e = \left(\frac{1}{6L_0} \sqrt{\sum_{n=1}^{6} (x_n' - x_n^{NN})^2 + (y_n' - y_n^{NN})^2} \right) \times 100\% \tag{1}$$

where L_0 is the median pitch of the entire BCP dot array; x_n^{NN} and y_n^{NN} are the x, y coordinates of the six nearest neighbors (sorted in a clockwise fashion), respectively; and x_n' and y_n' are the coordinates of the regular hexagon (with a pitch equal to L_0) that minimizes the value of R_e. Further detail of how R_e is calculated is given in the Supporting Information.

This effect of increased lattice deviations from perfect hexagonal coordination shells is illustrated in Figure 4 for an initial film thickness of 28.0 nm. At a low swelling degree of 1.6, the lattice has a very large number of point defects, but the number of defects sharply decreases as the swelling degree is increased to 1.8, at which point almost all of the point defects belong to the grain boundaries. However, as the swelling degree is further increased, a very subtle but important change can be observed in the R_e maps, where the map appears to be darker purple (higher registration error) despite a similar

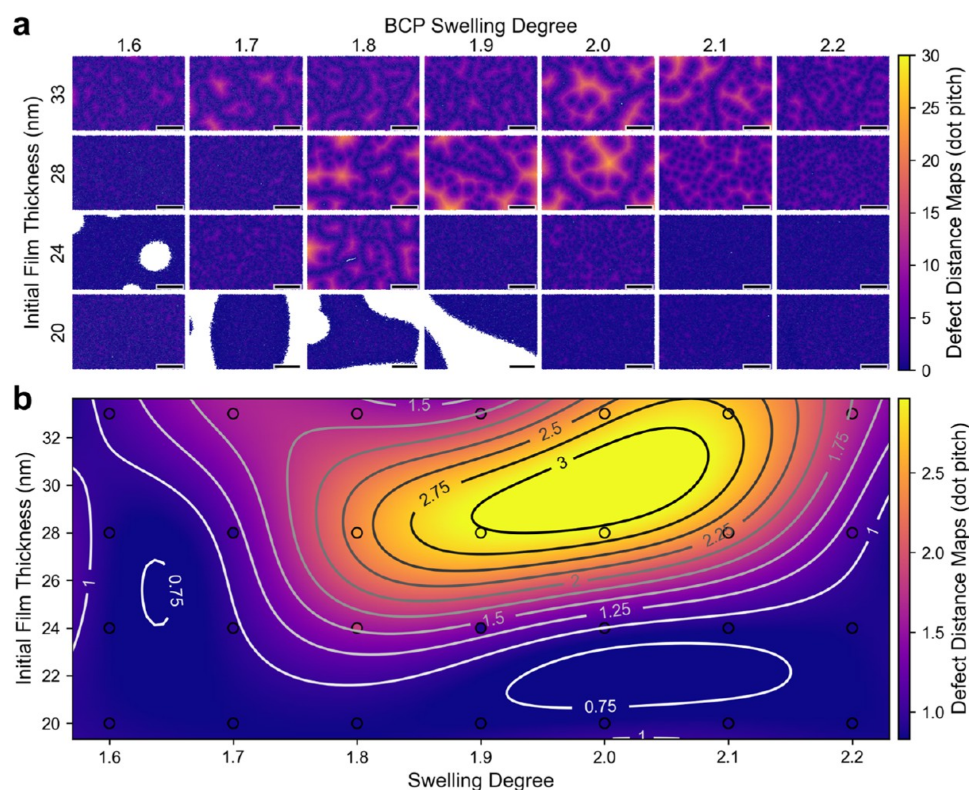

Figure 5. Defect distance as a function of SVA conditions. (a) Dot maps where the color value is the distance to the nearest defect. A defect is defined as having a registration error less than 17% where all of the vacancies and grain boundaries are included. All scale bars are 1 μm. (b) Support vector machine fitting using a radial basis function kernel of the effective defect distance per SVA condition.

number of point defects/grain boundaries. This increase of registration error is due to the average value of R_e increasing due to increased fluctuations in the local hexagonal coordination shell of BCP dots. This increase in the average R_e for 6-fold coordinated sites is believed to be a result of the decreasing segregation strength as the swelling degree increases.

Using this measure of registration error, we can define what constitutes a fluctuational defect in a physically meaningful way, as it relates to positional accuracy. Traditional measures of hexagonal lattice fluctuations, such as the local orientational order parameter, ψ_6,[72] are also very sensitive to fluctuations in hexagonal ordering, where mappings of ψ_6 are shown in Figure S5 and are very similar in appearance to the R_e mappings in Figure 4. However, there is no good way to relate values of ψ_6 to the possibility of a fluctuational defect, outside of choosing an arbitrary cutoff. Conversely, since R_e is a measure of actual distance, we can define a fluctuational defect when $R_e > r_0/L_0 \times 100$, where r_0 is the effective diameter of the BCP dots. From SEM data, we estimate the average dot size to be ~8 nm (see Figure S6), which is an overestimation due to charging effects and nonzero spot size of the electron beam. To more accurately estimate the true/effective size of the dots, we assume that they are at least 2 nm smaller than measured by SEM, giving an effective dot radius of ~6 nm. Therefore, all dots with a $R_e > 17$ are defined as a fluctuational (or point) defect. The physical interpretation of this defect definition is clear: if a read/write head is moved to the expected location of the nearest neighbor (based on a perfect hexagonal lattice) and the registration error is greater than 17%, the dot will not be detected. This definition of registration error is similar to the "jitter" model used in bit-patterned media, where a bit is considered to be written incorrectly if its effective jitter/excursion places it in its neighbor's write window.[73]

Having defined defects as above (counting both point and fluctuational defects), we would like to compute an appropriate figure of merit (FOM) for a given BCP dot array, which measures how desirable that BCP array would be if used for DSA having sparse lithographic definition. Although a raw average of the defect density is informative and simple to measure, it does not tell us how the defects are distributed in space. For instance, are they all located on grain boundaries or are they uniformly distributed throughout? As such, we define the metric of local defect distance, which is simply the minimum distance between a BCP dot and a defect (normalized by BCP pitch). Shown in Figure 5 are the local defect distance maps for each SVA condition tested. It is worth noting that these local defect distance maps are simply the Euclidean distance transform[74] of the defect maps (Figure S7). In contrast to the R_e maps, the local defect distance maps show that, from a patterned device perspective, better BCP arrays can be made from films with initial thicknesses of 28 nm, compared to 33 nm (i.e., there are much larger regions that do not contain any defects).

This metric of defect distance can be used to provide a lower-bound estimate for the minimum spacing between DSA guiding features necessary to produce defect-free patterns. A map of the effective defect distance (as a function of SVA conditions) is shown in Figure 5b, which clearly identifies a narrow region of optimal annealing conditions centered around an initial thickness of ~30 nm and swelling degree of ~2.0.

The phase behavior of dot-forming BCP thin films (such as PS-*b*-PDMS used in this work) is quite complex, as lamellae/

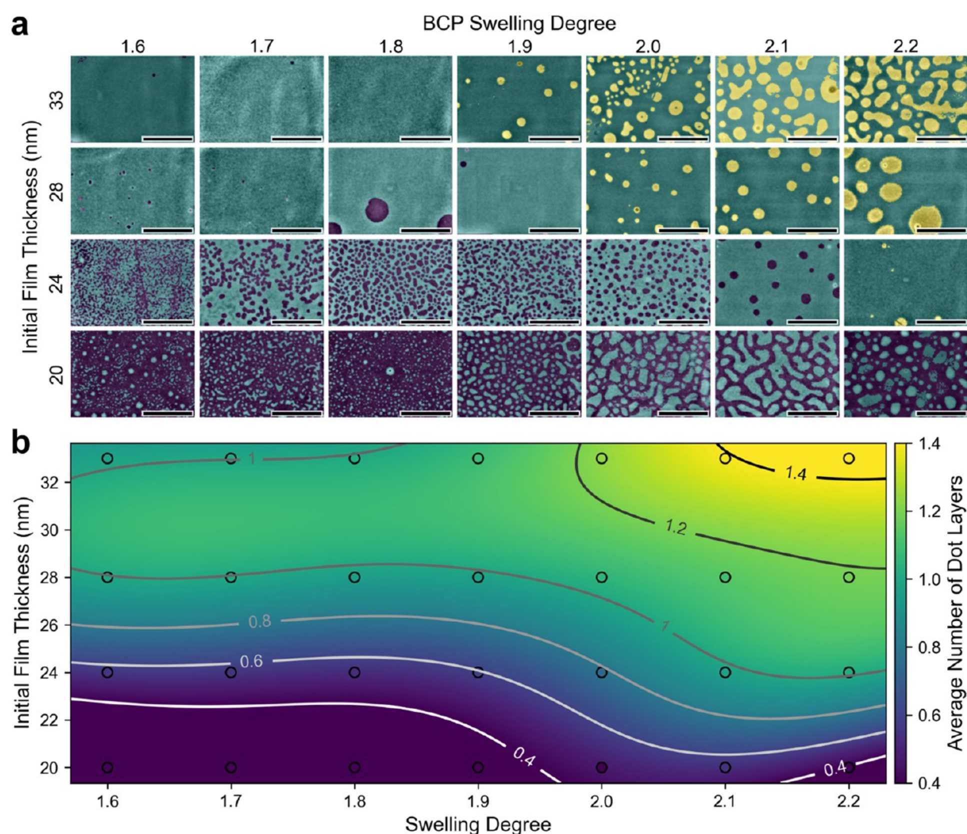

Figure 6. Number of hexagonal dot layers as a function of SVA conditions. (a) False-color low-magnification SEM micrographs showing wetting layers in dark blue, single layers in green, and double layers in yellow. All scale bars are 50 μm. (b) Support vector machine fitting using a radial basis function kernel of the area-averaged number of dot layers, where "0" represents a wetting layer, "1" represents a single layer of dots, and "2" represents double layer areas. The scale bar is set to 0.4−1.4 to improve contrast.

wetting layers and single layer hexagonal or multiple stacked layers of hexagonal dots can be formed. Which phases form in a BCP thin film is strongly dependent on initial thickness, which needs to be commensurate with the native BCP pitch.[47,48] Moreover, during SVA, the film swells in thickness, often resulting in the formation of multiple layers.[31,56] The nonuniformity of the thickness of the BCP films, as well as the mass transport of the solvent vapor during the annealing, plays critical roles regarding the formation of single, double, or wetting layers or bare exposed silicon.[31,50,56] The dot-forming BCP used here leads to a greater degree of single layers for thicker films at a lower degree of swelling; as the degree of swelling increases, however, more double layers are observed. Thinner films, on the other hand, have more single layers and wetting layers (or bare silicon) because there is insufficient BCP to form a continuous single layer of dots over the surface.[34] The final areal fraction of single layers (or desired phase) over the entire substrate is one of the most important (and often unreported) metrics of BCP thin film annealing. From the perspective of devices defined using DSA, any regions that are not the desired phase would effectively consist of 100% defects.

Shown in Figure 6a are false-colored low-magnification SEM images (100 μm × 100 μm), where purple shows lamellae/wetting layers, green is a single layer, and yellow is a double layer. The first thing to note is that under almost all SVA conditions there are generally two phases present, either a combination of lamellae/wetting and single layer phases or single layer and double layer phases. To better understand this phase behavior, the average number of layers (per SVA condition) is measured as

$$N_{\mathrm{ave}} = 0 \times f_{\mathrm{l}} + 1 \times f_{\mathrm{s}} + 2 \times f_{\mathrm{d}} \quad (2)$$

where f_l is the area fraction of lamellae, f_s is the fraction of single layers, and f_d is the fraction of double layers. Shown in Figure 6b is an ML fit to the average number of layers, as a function of SVA conditions, which reveals several important features of the phase formation. As expected, we see that the average number of layers generally increases as the initial thickness and swelling degree increase. However, at swelling degrees less than ∼1.8, the average number of layers is essentially insensitive to changes in the swelling degree, which is likely due to the very slow kinetics at these swelling degrees. One of the most useful features of this map is identifying the SVA conditions where the average layer number is close to 1.0 and is insensitive to fluctuations in SVA conditions. Specifically, from a practical device manufacturing perspective, there will always be nonuniformities in film thickness, mass transport, and solvent uptake over the entire substrate.[33] As such, it is important to consider these system sensitivities to inputs when selecting SVA conditions, where regions of a plateau with an average layer number of 1.0 are most desirable.

Making use of all of the above analysis, we can define a single FOM that can be used to identify the optimal SVA conditions for producing BCP dot arrays for patterned devices. The FOM we choose is simply the defect distance, modified by the fraction of single layers, as we need to proportionally reduce the effective defect distance to account for the fact that

https://doi.org/10.1021/acsami.1c05056
ACS Appl. Mater. Interfaces 2021, 13, 28639−28649

non-single-layer regions have a 100% defect density. A map of this FOM is shown in Figure 7c, which is the product of the defect distance (Figure 7a) and the fraction of a single layer (Figure 7b). It is noted that the optimal FOM does not correspond to either the optimal defect distance or single layer fraction regions but is rather the intersection of these two regions. This conclusion highlights the tradeoff between single layer fraction and defect distance: at lower swelling degrees, there is a large region of near 100% single layer, but the defectivity is much worse compared to that observed at higher swelling degrees. At higher swelling degrees, however, the decrease in defectivity is offset by a reduction in the number of single layers. This leads to a relatively narrow region of SVA conditions with the optimal FOM, which is located between a swelling degree of 1.9 and 2.0 and an initial film thickness of 28 and 30 nm. These conditions are clearly specific to this BCP with this molecular weight, but the methods presented here are completely general and can be utilized for different BCPs.

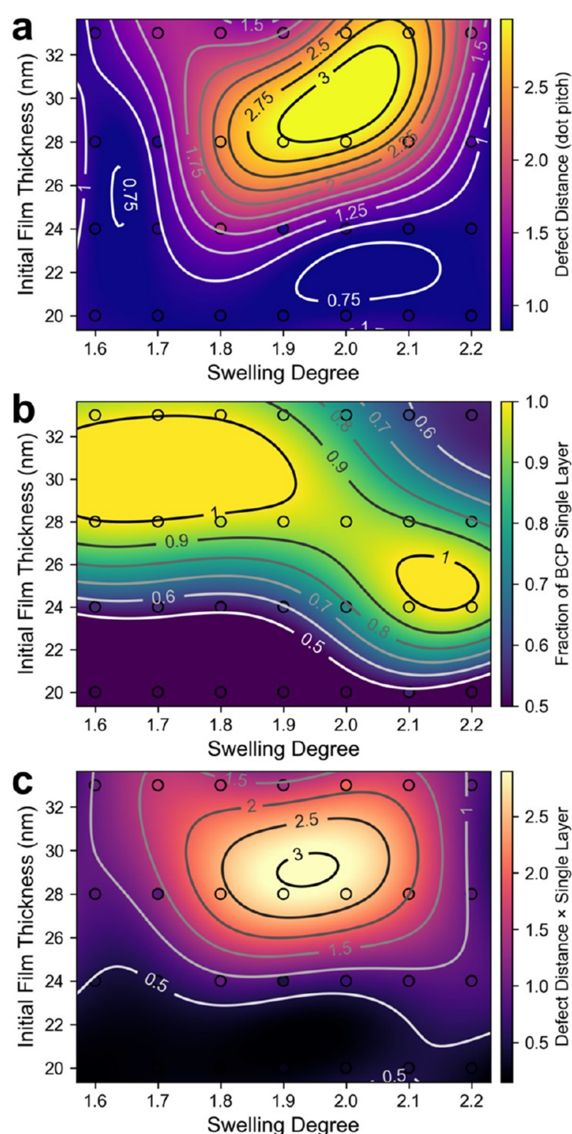

Figure 7. Support vector machine fitting using a radial basis function kernel of the (a) the 20th percentile of defective distance per SVA condition (where a defect is defined as having a registration error above 17% where the majority of the vacancies and grain boundaries are included). (b) Single layer fraction and (c) multiplication of single layer fraction by defect distance.

Shown in Figure S8 are the prediction fits of the ML algorithm to the measured values including the FOM. Given the excellent prediction of the ML fit to the data, this figure suggests that the ground truth map of the FOM has a similar level of smoothness/bandwidth as that shown in Figure 7c. This is valuable information from an experimental optimization point of view, as it reveals that further experiments at different swelling degrees or initial thickness are unlikely to yield much higher FOMs. The knowledge gained from the ML fitting and visualization represents significant time savings for the experimentalist, as further experiments are likely to produce only marginal increases in the desired FOM.

Although not presented in this work, several further refinements/modifications of this method can be applied for the SVA optimization of nanopatterns derived from BCP films. As presented in our previous work on optimization of thin-film organic photovoltaic cells,[59] the coupling of DOE with ML, done in an iterative manner, can be a very powerful tool for optimization. Specifically, in this work, we have carried out what would be considered a full factorial design, where the parameter space is sampled uniformly on a dense grid. The number of experiments could be reduced by applying a generalized subset design[75] and still perform the ML fitting to identify regions of interest with a high FOM. These regions could then be further sampled using DOE + ML in an iterative fashion. Furthermore, once the first round of optimization was done to identify these promising regions, even greater FOMs could be achieved if the annealing time was investigated in these regions, as longer annealing times will likely reduce defectivity in the films.

SUMMARY

The application of block copolymer self-assembly for pattern generation with a sublithographic resolution requires minimization of defect densities at both the nano- and macroscales. Controlling and optimizing a large number of correlated and convoluted process parameters during processing and subsequent data analysis are time consuming if executed in an empirical fashion and may not arrive at the optimum conditions. In this work, we investigated the influence of the small thickness variations and swelling degrees on the final morphology of the BCP patterns and how to optimize these SVA parameters for the fabrication of devices. A full factorial experimental design was used to probe the SVA parameter space, and a figure of merit was formulated to evaluate the quality of the resultant BCP nanopatterns, accounting for multiple length scales and the requirements of patterned devices. Machine learning was then utilized to fit the SVA parameter space and identify the optimal annealing conditions with respect to the figure of merit. This approach is generalizable to optimize, analyze, and arrive at predictions of defect densities for different combinations of materials and processes for device fabrication. This combination of techniques may be applied to any combination of materials and processes to optimize, analyze, predict, and minimize the defect densities in any given pattern.

ASSOCIATED CONTENT

Supporting Information

The Supporting Information is available free of charge at https://pubs.acs.org/doi/10.1021/acsami.1c05056.

Plots showing the relationship between initial film thickness and the concentration of the BCP solution; SEM micrographs of BCP dot patterns; low-magnification SEM micrographs colored by the BCP phase; ML maps and/or dot maps as a function of the swelling degree and initial film thickness of BCP pitch, coordination number, orientational order parameter, and fluctuational defects; and histograms of BCP dot size, registration error, BCP cell orientation, BCP pitch, and defect distance; and prediction fits of the ML models (PDF)

AUTHOR INFORMATION

Corresponding Authors

Erik J. Luber − *Department of Chemistry, University of Alberta, Edmonton, Alberta T6G 2G2, Canada;* orcid.org/0000-0003-1623-0102; Email: eluber@ualberta.ca

Jillian M. Buriak − *Department of Chemistry, University of Alberta, Edmonton, Alberta T6G 2G2, Canada;* orcid.org/0000-0002-9567-4328; Email: jburiak@ualberta.ca

Authors

Gayashani Ginige − *Department of Chemistry, University of Alberta, Edmonton, Alberta T6G 2G2, Canada;* orcid.org/0000-0002-4434-9648

Youngdong Song − *Department of Chemical and Biomolecular Engineering, Korea Advanced Institute of Science and Technology (KAIST), Daejeon 34141, Republic of Korea*

Brian C. Olsen − *Department of Chemistry, University of Alberta, Edmonton, Alberta T6G 2G2, Canada;* orcid.org/0000-0001-9758-3641

Cafer T. Yavuz − *Department of Chemical and Biomolecular Engineering, Korea Advanced Institute of Science and Technology (KAIST), Daejeon 34141, Republic of Korea; KAUST Catalysis Center (KCC), Physical Sciences and Engineering (PSE), King Abdullah University of Science and Technology (KAUST), Thuwal 23955-6900, Saudi Arabia; Advanced Membranes and Porous Materials Center (AMPM), Physical Sciences and Engineering (PSE), King Abdullah University of Science and Technology (KAUST), Thuwal 23955-6900, Saudi Arabia;* orcid.org/0000-0003-0580-3331

Complete contact information is available at: https://pubs.acs.org/10.1021/acsami.1c05056

Notes

The authors declare no competing financial interest.

ACKNOWLEDGMENTS

This work was supported by NSERC (grant number RGPIN-2018-04294), Alberta Innovates Technology Futures (grant number AITF iCORE IC50-T1 G2013000198), the Canada Research Chairs program (CRC 207142), and the International Research & Development Program of the National Research Foundation of Korea (NRF) funded by the Ministry of Science and ICT (grant number 2017K1A3A1A12029286). The University of Alberta Centre for Nanofabrication (the nanoFAB) and the National Research Council-Edmonton are thanked for the use of facilities.

REFERENCES

(1) Chen, Y.; Xiong, S. Directed Self-Assembly of Block Copolymers for Sub-10 nm Fabrication. *Int. J. Extrem. Manuf.* **2020**, *2*, No. 032006.

(2) Liu, C.-C.; Franke, E.; Mignot, Y.; Xie, R.; Yeung, C. W.; Zhang, J.; Chi, C.; Zhang, C.; Farrell, R.; Lai, K.; Tsai, H.; Felix, N.; Corliss, D. Directed Self-Assembly of Block Copolymers for 7 Nanometer FinFET Technology and Beyond. *Nat. Electron.* **2018**, *1*, 562−569.

(3) Liu, C.-C.; Mignot, Y.; Chi, C.; Farrell, R.; Lai, K.; Guo, J.; Sha, J.; Glodde, M.; Muramatsu, M.; Ido, Y.; Felix, N.; Hetzer, D.; Metz, A.; Corliss, D. In *The Integration of 193i and DSA for BEOL Metal Cuts/Blocks Targeting Sub-20 nm Tip-to-Tip CD*, Novel Patterning Technologies 201; International Society for Optics and Photonics, 2018; Vol. 10584, 105840L.

(4) Stein, A.; Wright, G.; Yager, K. G.; Doerk, G. S.; Black, C. T. Selective Directed Self-Assembly of Coexisting Morphologies Using Block Copolymer Blends. *Nat. Commun.* **2016**, *7*, No. 12366.

(5) Arias-Zapata, J.; Böhme, S.; Garnier, J.; Girardot, C.; Legrain, A.; Zelsmann, M. Ultrafast Assembly of PS-PDMS Block Copolymers on 300 mm Wafers by Blending with Plasticizers. *Adv. Funct. Mater.* **2016**, *26*, 5690−5700.

(6) Kim, J. Y.; Liu, P.; Maher, M. J.; Callan, D. H.; Bates, C. M.; Carlson, M. C.; Asano, Y.; Blachut, G.; Rettner, C. T.; Cheng, J. Y.; Sunday, D. F.; Kline, R. J.; Sanders, D. P.; Lynd, N. A.; Ellison, C. J.; Willson, C. G.; Baiz, C. R. Spatial Control of the Self-Assembled Block Copolymer Domain Orientation and Alignment on Photopatterned Surfaces. *ACS Appl. Mater. Interfaces* **2020**, *12*, 23399−23409.

(7) Li, W.; Müller, M. Directed Self-Assembly of Block Copolymers by Chemical or Topographical Guiding Patterns: Optimizing Molecular Architecture, Thin-Film Properties, and Kinetics. *Prog. Polym. Sci.* **2016**, *54-55*, 47−75.

(8) Frascaroli, J.; Brivio, S.; Ferrarese Lupi, F.; Seguini, G.; Boarino, L.; Perego, M.; Spiga, S. Resistive Switching in High-Density Nanodevices Fabricated by Block Copolymer Self-Assembly. *ACS Nano* **2015**, *9*, 2518−2529.

(9) Li, D.; Chien, C.; Wei, X.; Huang, Y.; Qu, X.; Chang, T.; Xiong, S. In *Sub-10 nm Silicon FinFET Devices on SOI Substrate Made by Block Copolymer Lithography*, 2018 14th IEEE International Conference on Solid-State and Integrated Circuit Technology (ICSICT), 2018; pp 1−3.

(10) Murugesan, M.; Fukushima, T.; Bea, J. C.; Hashimoto, H.; Koyanagi, M. *Intra- and Inter-Chip Electrical Interconnection Formed by Directed Self Assembly of Nanocomposite Containing Diblock Copolymer and Nanometal*, 2018 IEEE International Reliability Physics Symposium (IRPS), 2018; pp 4D.2-1−4D.2-7.

(11) Rottler, J.; Müller, M. Kinetic Pathways of Block Copolymer Directed Self-Assembly: Insights from Efficient Continuum Modeling. *ACS Nano* **2020**, *14*, 13986−13994.

(12) Kim, J. Y.; Lim, J.; Jin, H. M.; Kim, B. H.; Jeong, S.-J.; Choi, D. S.; Li, D. J.; Kim, S. O. 3D Tailored Crumpling of Block-Copolymer Lithography on Chemically Modified Graphene. *Adv. Mater.* **2016**, *28*, 1591−1596.

(13) Wei, W.; Samad, L.; Choi, J. W.; Joo, Y.; Way, A.; Arnold, M. S.; Jin, S.; Gopalan, P. Synthesis of Molybdenum Disulfide Nanowire Arrays Using a Block Copolymer Template. *Chem. Mater.* **2016**, *28*, 4017−4023.

(14) Stel, B.; Gunkel, I.; Gu, X.; Russell, T. P.; De Yoreo, J. J.; Lingenfelder, M. Contrasting Chemistry of Block Copolymer Films Controls the Dynamics of Protein Self-Assembly at the Nanoscale. *ACS Nano* **2019**, *13*, 4018−4027.

(15) Xie, T.; Chattoraj, J.; Mulcahey, P. J.; Kelleher, N. P.; Gado, E. D.; Hahm, J. Revealing the Principal Attributes of Protein Adsorption on Block Copolymer Surfaces with Direct Experimental Evidence at the Single Protein Level. *Nanoscale* **2018**, *10*, 9063−9076.

(16) Zhu, G.; Ying, Y.; Li, X.; Liu, Y.; Yang, C.; Yi, Z.; Gao, C. Isoporous Membranes with Sub-10 nm Pores Prepared from Supramolecular Interaction Facilitated Block Copolymer Assembly

https://doi.org/10.1021/acsami.1c05056
ACS Appl. Mater. Interfaces 2021, 13, 28639−28649

and Application for Protein Separation. *J. Membr. Sci.* **2018**, *566*, 25−34.
(17) Zhou, C.; Segal-Peretz, T.; Oruc, M. E.; Suh, H. S.; Wu, G.; Nealey, P. F. Fabrication of Nanoporous Alumina Ultrafiltration Membrane with Tunable Pore Size Using Block Copolymer Templates. *Adv. Funct. Mater.* **2017**, *27*, No. 1701756.
(18) Jin, H. M.; Kim, J. Y.; Heo, M.; Jeong, S.-J.; Kim, B. H.; Cha, S. K.; Han, K. H.; Kim, J. H.; Yang, G. G.; Shin, J.; Kim, S. O. Ultralarge Area Sub-10 nm Plasmonic Nanogap Array by Block Copolymer Self-Assembly for Reliable High-Sensitivity SERS. *ACS Appl. Mater. Interfaces* **2018**, *10*, 44660−44667.
(19) Akinoglu, G. E.; Mir, S. H.; Gatensby, R.; Rydzek, G.; Mokarian-Tabari, P. Block Copolymer Derived Vertically Coupled Plasmonic Arrays for Surface-Enhanced Raman Spectroscopy. *ACS Appl. Mater. Interfaces* **2020**, *12*, 23410−23416.
(20) Adak, D.; Ghosh, S.; Chakraborty, P.; Srivatsa, K. M. K.; Mondal, A.; Saha, H.; Mukherjee, R.; Bhattacharyya, R. Non Lithographic Block Copolymer Directed Self-Assembled and Plasma Treated Self-Cleaning Transparent Coating for Photovoltaic Modules and Other Solar Energy Devices. *Sol. Energy Mater. Sol. Cells* **2018**, *188*, 127−139.
(21) Mokarian-Tabari, P.; Senthamaraikannan, R.; Glynn, C.; Collins, T. W.; Cummins, C.; Nugent, D.; O'Dwyer, C.; Morris, M. A. Large Block Copolymer Self-Assembly for Fabrication of Subwavelength Nanostructures for Applications in Optics. *Nano Lett.* **2017**, *17*, 2973−2978.
(22) Wei, S.; Tian, F.; Ge, F.; Wang, X.; Zhang, G.; Lu, H.; Yin, J.; Wu, Z.; Qiu, L. Helical Nanofibrils of Block Copolymer for High-Performance Ammonia Sensors. *ACS Appl. Mater. Interfaces* **2018**, *10*, 22504−22512.
(23) Bas, S. Z.; Cummins, C.; Selkirk, A.; Borah, D.; Ozmen, M.; Morris, M. A. A Novel Electrochemical Sensor Based on Metal Ion Infiltrated Block Copolymer Thin Films for Sensitive and Selective Determination of Dopamine. *ACS Appl. Nano Mater.* **2019**, *2*, 7311−7318.
(24) Nagpal, U.; Müller, M.; Nealey, P. F.; de Pablo, J. J. Free Energy of Defects in Ordered Assemblies of Block Copolymer Domains. *ACS Macro Lett.* **2012**, *1*, 418−422.
(25) Li, W.; Müller, M. Thermodynamics and Kinetics of Defect Motion and Annihilation in the Self-Assembly of Lamellar Diblock Copolymers. *Macromolecules* **2016**, *49*, 6126−6138.
(26) Hur, S.-M.; Thapar, V.; Ramírez-Hernández, A.; Nealey, P. F.; de Pablo, J. J. Defect Annihilation Pathways in Directed Assembly of Lamellar Block Copolymer Thin Films. *ACS Nano* **2018**, *12*, 9974−9981.
(27) Doise, J.; Koh, J. H.; Kim, J. Y.; Zhu, Q.; Kinoshita, N.; Suh, H. S.; Delgadillo, P. R.; Vandenberghe, G.; Willson, C. G.; Ellison, C. J. Strategies for Increasing the Rate of Defect Annihilation in the Directed Self-Assembly of High-χ Block Copolymers. *ACS Appl. Mater. Interfaces* **2019**, *11*, 48419−48427.
(28) International Technology Roadmap for Semiconductors, 2011th ed.; Semiconductor Industry Association: San Jose, CA, 2011, https://www.semiconductors.org/resources/2011-international-technology-roadmap-for-semiconductors-itrs/.
(29) Hur, S.-M.; Khaira, G. S.; Ramírez-Hernández, A.; Müller, M.; Nealey, P. F.; de Pablo, J. J. Simulation of Defect Reduction in Block Copolymer Thin Films by Solvent Annealing. *ACS Macro Lett.* **2015**, *4*, 11−15.
(30) Gu, X.; Gunkel, I.; Hexemer, A.; Gu, W.; Russell, T. P. An In Situ Grazing Incidence X-Ray Scattering Study of Block Copolymer Thin Films During Solvent Vapor Annealing. *Adv. Mater.* **2014**, *26*, 273−281.
(31) Jin, C.; Olsen, B. C.; Luber, E. J.; Buriak, J. M. Nanopatterning via Solvent Vapor Annealing of Block Copolymer Thin Films. *Chem. Mater.* **2017**, *29*, 176−188.
(32) Selkirk, A.; Prochukhan, N.; Lundy, R.; Cummins, C.; Gatensby, R.; Kilbride, R.; Parnell, A.; Baez Vasquez, J.; Morris, M.; Mokarian-Tabari, P. Optimization and Control of Large Block Copolymer Self-Assembly via Precision Solvent Vapor Annealing. *Macromolecules* **2021**, 1203−1215.
(33) Williamson, L. D.; Seidel, R. N.; Chen, X.; Suh, H. S.; Rincon Delgadillo, P.; Gronheid, R.; Nealey, P. F. Three-Tone Chemical Patterns for Block Copolymer Directed Self-Assembly. *ACS Appl. Mater. Interfaces* **2016**, *8*, 2704−2712.
(34) Kim, S.-W.; Kim, E.; Lee, H.; Berry, B. C.; Kim, H.-C.; Ryu, D. Y. Thickness-Dependent Ordering of Perpendicularly Oriented Lamellae in PS-*b*-PMMA Thin Films. *Polymer* **2015**, *74*, 63−69.
(35) Jin, C.; Murphy, J. N.; Harris, K. D.; Buriak, J. M. Deconvoluting the Mechanism of Microwave Annealing of Block Copolymer Thin Films. *ACS Nano* **2014**, *8*, 3979−3991.
(36) Borah, D.; Shaw, M. T.; Holmes, J. D.; Morris, M. A. Sub-10 nm Feature Size PS-b-PDMS Block Copolymer Structures Fabricated by a Microwave-Assisted Solvothermal Process. *ACS Appl. Mater. Interfaces* **2013**, *5*, 2004−2012.
(37) Cummins, C.; Mokarian-Tabari, P.; Andreazza, P.; Sinturel, C.; Morris, M. A. Solvothermal Vapor Annealing of Lamellar Poly(styrene)-*Block*-Poly(d,l-Lactide) Block Copolymer Thin Films for Directed Self-Assembly Application. *ACS Appl. Mater. Interfaces* **2016**, *8*, 8295−8304.
(38) Majewski, P. W.; Yager, K. G. Millisecond Ordering of Block Copolymer Films via Photothermal Gradients. *ACS Nano* **2015**, *9*, 3896−3906.
(39) Leniart, A. A.; Pula, P.; Sitkiewicz, A.; Majewski, P. W. Macroscopic Alignment of Block Copolymers on Silicon Substrates by Laser Annealing. *ACS Nano* **2020**, *14*, 4805−4815.
(40) Zhang, C.; Cavicchi, K. A.; Li, R.; Yager, K. G.; Fukuto, M.; Vogt, B. D. Thickness Limit for Alignment of Block Copolymer Films Using Solvent Vapor Annealing with Shear. *Macromolecules* **2018**, *51*, 4213−4219.
(41) Luo, M.; Scott, D. M.; Epps, T. H. Writing Highly Ordered Macroscopic Patterns in Cylindrical Block Polymer Thin Films via Raster Solvent Vapor Annealing and Soft Shear. *ACS Macro Lett.* **2015**, *4*, 516−520.
(42) Jo, S.; Jeon, S.; Kim, H.; Ryu, C. Y.; Lee, S.; Ryu, D. Y. Balanced Interfacial Interactions for Fluoroacrylic Block Copolymer Films and Fast Electric Field Directed Assembly. *Chem. Mater.* **2020**, *32*, 9633−9641.
(43) Ober, C. K. A Dress Code for Block Copolymers. *Nat. Nanotechnol.* **2017**, *12*, 507−508.
(44) Suh, H. S.; Kim, D. H.; Moni, P.; Xiong, S.; Ocola, L. E.; Zaluzec, N. J.; Gleason, K. K.; Nealey, P. F. Sub-10-nm Patterning via Directed Self-Assembly of Block Copolymer Films with a Vapour-Phase Deposited Topcoat. *Nat. Nanotechnol.* **2017**, *12*, 575−581.
(45) Michman, E.; Langenberg, M.; Stenger, R.; Oded, M.; Schvartzman, M.; Müller, M.; Shenhar, R. Controlled Spacing Between Nanopatterned Regions in Block Copolymer Films Obtained by Utilizing Substrate Topography for Local Film Thickness Differentiation. *ACS Appl. Mater. Interfaces* **2019**, *11*, 35247−35254.
(46) Shin, J. Y.; Oh, Y. T.; Kim, S.; Lim, H. Y.; Lee, B.; Ko, Y. C.; Park, S.; Seon, S. W.; Lee, S. G.; Mun, S. S.; Kim, B. H. Hierarchical Self-Assembly of Thickness-Modulated Block Copolymer Thin Films for Controlling Nanodomain Orientations Inside Bare Silicon Trenches. *Polymers* **2021**, *13*, No. 553.
(47) Ham, S.; Shin, C.; Kim, E.; Ryu, D. Y.; Jeong, U.; Russell, T. P.; Hawker, C. J. Microdomain Orientation of PS-b-PMMA by Controlled Interfacial Interactions. *Macromolecules* **2008**, *41*, 6431−6437.
(48) Smith, A. P.; Douglas, J. F.; Meredith, J. C.; Amis, E. J.; Karim, A. Combinatorial Study of Surface Pattern Formation in Thin Block Copolymer Films. *Phys. Rev. Lett.* **2001**, *87*, No. 015503.
(49) Kim, B. H.; Lee, H. M.; Lee, J.-H.; Son, S.-W.; Jeong, S.-J.; Lee, S.; Lee, D. I.; Kwak, S. U.; Jeong, H.; Shin, H.; Yoon, J.-B.; Lavrentovich, O. D.; Kim, S. O. Spontaneous Lamellar Alignment in Thickness-Modulated Block Copolymer Films. *Adv. Funct. Mater.* **2009**, *19*, 2584−2591.

(50) Black, C. T.; Forrey, C.; Yager, K. G. Thickness-Dependence of Block Copolymer Coarsening Kinetics. *Soft Matter* **2017**, *13*, 3275–3283.
(51) Olaya-Muñoz, D. A.; Nealey, P. F.; Hernández-Ortiz, J. P. Leveling of Polymer Grating Structures Upon Heating: Dimension Dependence on the Nanoscale and the Effect of Antiplasticizers. *ACS Appl. Mater. Interfaces* **2018**, *10*, 27432–27443.
(52) Ren, J.; Zhou, C.; Chen, X.; Dolejsi, M.; Craig, G. S. W.; Rincon Delgadillo, P. A.; Segal-Peretz, T.; Nealey, P. F. Engineering the Kinetics of Directed Self-Assembly of Block Copolymers Toward Fast and Defect-Free Assembly. *ACS Appl. Mater. Interfaces* **2018**, *10*, 23414–23423.
(53) Knoll, A.; Horvat, A.; Lyakhova, K. S.; Krausch, G.; Sevink, G. J. A.; Zvelindovsky, A. V.; Magerle, R. Phase Behavior in Thin Films of Cylinder-Forming Block Copolymers. *Phys. Rev. Lett.* **2002**, *89*, No. 035501.
(54) Sunday, D. F.; Dolejsi, M.; Chang, A. B.; Richter, L. J.; Li, R.; Kline, R. J.; Nealey, P. F.; Grubbs, R. H. Confinement and Processing Can Alter the Morphology and Periodicity of Bottlebrush Block Copolymers in Thin Films. *ACS Nano* **2020**, *14*, 17476–17486.
(55) Li, W.; Müller, M. Defects in the Self-Assembly of Block Copolymers and Their Relevance for Directed Self-Assembly. *Annu. Rev. Chem. Biomol. Eng.* **2015**, *6*, 187–216.
(56) Knoll, A.; Magerle, R.; Krausch, G. Phase Behavior in Thin Films of Cylinder-Forming ABA Block Copolymers: Experiments. *J. Chem. Phys.* **2004**, *120*, 1105–1116.
(57) Harrison, C.; Angelescu, D. E.; Trawick, M.; Cheng, Z.; Huse, D. A.; Chaikin, P. M.; Vega, D. A.; Sebastian, J. M.; Register, R. A.; Adamson, D. H. Pattern Coarsening in a 2D Hexagonal System. *Europhys. Lett.* **2004**, *67*, 800.
(58) Vega, D. A.; Harrison, C. K.; Angelescu, D. E.; Trawick, M. L.; Huse, D. A.; Chaikin, P. M.; Register, R. A. Ordering Mechanisms in Two-Dimensional Sphere-Forming Block Copolymers. *Phys. Rev. E* **2005**, *71*, No. 061803.
(59) Cao, B.; Adutwum, L. A.; Oliynyk, A. O.; Luber, E. J.; Olsen, B. C.; Mar, A.; Buriak, J. M. How to Optimize Materials and Devices via Design of Experiments and Machine Learning: Demonstration Using Organic Photovoltaics. *ACS Nano* **2018**, *12*, 7434–7444.
(60) Kirkey, A.; Luber, E. J.; Cao, B.; Olsen, B. C.; Buriak, J. M. Optimization of the Bulk Heterojunction of All-Small-Molecule Organic Photovoltaics Using Design of Experiment and Machine Learning Approaches. *ACS Appl. Mater. Interfaces* **2020**, *12*, 54596–54607.
(61) Nečas, D.; Klapetek, P. Gwyddion: An Open-Source Software for SPM Data Analysis. *Open Phys.* **2011**, *10*, 181–188.
(62) Otsu, N. A Threshold Selection Method from Gray-Level Histograms. *IEEE Trans. Syst. Man Cybern.* **1979**, *9*, 62–66.
(63) Pedregosa, F.; Varoquaux, G.; Gramfort, A.; Michel, V.; Thirion, B.; Grisel, O.; Blondel, M.; Prettenhofer, P.; Weiss, R.; Dubourg, V.; Vanderplas, J.; Passos, A.; Cournapeau, D.; Brucher, M.; Perrot, M.; Duchesnay, E Scikit-Learn: Machine Learning in Python. *J. Mach. Learn. Res.* **2011**, *12*, 2825–2830.
(64) Jeong, J. W.; Park, W. I.; Kim, M.-J.; Ross, C. A.; Jung, Y. S. Highly Tunable Self-Assembled Nanostructures from a Poly(2-Vinylpyridine-*b*-Dimethylsiloxane) Block Copolymer. *Nano Lett.* **2011**, *11*, 4095–4101.
(65) Leibler, L. Theory of Microphase Separation in Block Copolymers. *Macromolecules* **1980**, *13*, 1602–1617.
(66) Jung, Y. S.; Ross, C. A. Solvent-Vapor-Induced Tunability of Self-Assembled Block Copolymer Patterns. *Adv. Mater.* **2009**, *21*, 2540–2545.
(67) Helfand, E.; Tagami, Y. Theory of the Interface Between Immiscible Polymers. II. *J. Chem. Phys.* **1972**, *56*, 3592–3601.
(68) Cheng, L.-C.; Bai, W.; Martin, E. F.; Tu, K.-H.; Ntetsikas, K.; Liontos, G.; Avgeropoulos, A.; Ross, C. A. Morphology, Directed Self-Assembly and Pattern Transfer from a High Molecular Weight Polystyrene-*Block*-Poly(dimethylsiloxane) Block Copolymer Film. *Nanotechnology* **2017**, *28*, No. 145301.
(69) Baruth, A.; Seo, M.; Lin, C. H.; Walster, K.; Shankar, A.; Hillmyer, M. A.; Leighton, C. Optimization of Long-Range Order in Solvent Vapor Annealed Poly(styrene)-*Block*-Poly(lactide) Thin Films for Nanolithography. *ACS Appl. Mater. Interfaces* **2014**, *6*, 13770–13781.
(70) Gasser, U.; Eisenmann, C.; Maret, G.; Keim, P. Melting of Crystals in Two Dimensions. *ChemPhysChem* **2010**, *11*, 963–970.
(71) Tiron, R.; Chevalier, X.; Couderc, C.; Pradelles, J.; Bustos, J.; Pain, L.; Navarro, C.; Magnet, S.; Fleury, G.; Hadziioannou, G. Optimization of Block Copolymer Self-Assembly Through Graphoepitaxy: A Defectivity Study. *J. Vac. Sci. Technol., B: Nanotechnol. Microelectron.: Mater., Process., Meas., Phenom.* **2011**, *29*, No. 06F206.
(72) Steinhardt, P. J.; Nelson, D. R.; Ronchetti, M. Bond-Orientational Order in Liquids and Glasses. *Phys. Rev. B* **1983**, *28*, 784–805.
(73) Albrecht, T. R.; Hellwing, O.; Ruiz, R.; Schabes, M. E.; Terris, B. D.; Wu, X. Z. Bit-Patterned Magnetic Recording: Nanoscale Magnetic Islands for Data Storage. In *Nanoscale Magnetic Materials and Applications*; Liu, J. P., Fullerton, E., Gutfleisch, O., Sellmyer, D. J., Eds.; Springer US: Boston, MA, 2009; pp 237–274.
(74) Danielsson, P.-E. Euclidean Distance Mapping. *Comput. Graph. Image Process.* **1980**, *14*, 227–248.
(75) Surowiec, I.; Vikström, L.; Hector, G.; Johansson, E.; Vikström, C.; Trygg, J. Generalized Subset Designs in Analytical Chemistry. *Anal. Chem.* **2017**, *89*, 6491–6497.